Journal of Geophysical Research: Atmospheres

RESEARCH ARTICLE
10.1029/2017JD028195

Enhanced Temperature-Humidity Similarity Caused by Entrainment Processes With Increased Wind Shear

Zhongming Gao[1], Heping Liu[1], Dan Li[2], Gabriel G. Katul[3,4], and Peter D. Blanken[5]

[1]Laboratory for Atmospheric Research, Department of Civil and Environmental Engineering, Washington State University, Pullman, WA, USA, [2]Department of Earth and Environment, Boston University, Boston, MA, USA, [3]Nicholas School of the Environment, Duke University, Durham, NC, USA, [4]Department of Civil and Environmental Engineering, Duke University, Durham, NC, USA, [5]Department of Geography, University of Colorado at Boulder, Boulder, CO, USA

Key Points:
- Similarity between temperature and humidity improved with increasing wind shear
- Temperature and humidity of large eddies became more synchronized with increased wind shear
- Enhanced temperature-humidity similarity was conjectured to be due to intensified entrainment of more synchronized, large cool/dry eddies at higher wind shear conditions

Correspondence to:
H. Liu,
heping.liu@wsu.edu

Citation:
Gao, Z., Liu, H., Li, D., Katul, G. G., & Blanken, P. D. (2018). Enhanced temperature-humidity similarity caused by entrainment processes with increased wind shear. *Journal of Geophysical Research: Atmospheres*, *123*. https://doi.org/10.1029/2017JD028195

Received 14 DEC 2017
Accepted 4 APR 2018
Accepted article online 16 APR 2018

Abstract A number of studies already suggested that entrainment of warm/dry air from aloft degrades the similarity between air temperature (T) and specific humidity (q) in the atmospheric surface layer (ASL). Less is known about entrainment of cool/dry air on the ASL T-q similarity. Using eddy covariance measurements over a large inland water surface, enhanced T-q similarity with increased friction velocity (u_*) was measured during daytime unstable conditions. Explaining this enhancement is the main goal of this work. Cool/dry air masses originating and advecting from land set the upper boundary condition on a quasi-equilibrated internal boundary layer embedding the warm/moist ASL over water. With increased u_*, the entrainment velocity ($dh_l/dt \propto u_*$) increases, thereby enhancing entrainment of cool/dry air originating from land, where t is time and h_l is the internal boundary layer depth. By analyzing the scale-dependent (spectral) correlation coefficients, the enhanced T-q similarity with increased u_* was shown to originate from spectral correlation coefficients in the middle- to low-frequency ranges (large eddies $\gg z$, the distance from the surface). With further increases in u_*, similarity between T and q within large eddies was further enhanced and phase differences between T and q was reduced. Quadrant analysis showed large increases in flux and time fractions of downward large cool/dry eddies with increasing u_*. These results provide evidence that enhanced entrainment of synchronized, large cool/dry eddies was a primary cause for the increased T-q similarity with increasing u_*.

1. Introduction

The similarity and dissimilarity of turbulent air temperature (T) and specific humidity (q) have long been the subject of active research in the atmospheric surface layer (ASL) (Andreas et al., 1998; Asanuma et al., 2007; de Bruin et al., 1999; Guo et al., 2009; Huang et al., 2013; Katul et al., 2016; Katul et al., 2008; Larsén et al., 2014; Li et al., 2012; Mahrt, 1991; McNaughton & Laubach, 1998; Moene & Schüttemeyer, 2008; Smedman et al., 2007). The occurrence of such temperature-humidity dissimilarity challenges the application of Monin-Obukhov similarity theory, including the use of flux-variance method to estimate latent heat flux once sensible heat flux is determined (Choi et al., 2004; de Bruin et al., 1999; Larsén et al., 2014; Li et al., 2012). A number of mechanisms have been proposed to explain the T-q dissimilarity, including the active role of temperature in the production of turbulence (Katul & Parlange, 1994), advection of heat and moisture (Assouline et al., 2008; Lee et al., 2004), surface heterogeneity in scalar sources and sinks (Andreas et al., 1998; Detto et al., 2008; Katul et al., 1995; Moene & Schüttemeyer, 2008; Williams et al., 2007), unsteadiness in the outer-layer flow (Högström, 1990; McNaughton & Laubach, 1998), and a number of entrainment processes (Asanuma et al., 2007; Cava et al., 2008; Choi et al., 2004; de Bruin et al., 1999; Katul et al., 2008; Mahrt, 1991; van de Boer et al., 2014) that communicate with the ASL via large and coherent structures (Huang et al., 2013; Li & Bou-Zeid, 2011). Among these mechanisms, entrainment is one common process leading to T-q dissimilarity (Katul et al., 2008).

Entrainment induced T-q dissimilarity is largely attributed to warm/dry air parcels from the outer layer characterized by a negative T-q correlation, which impinge on an ASL that experiences a positive T-q correlation originating from similarity in heat and water vapor sources at the boundary (typical for vegetated cover with both upward sensible and latent heat fluxes). Such impingement is expected to degrade the ASL T-q similarity if the top-down entrainment is sufficiently strong (Asanuma et al., 2007; Cava et al., 2008; Choi et al., 2004; de Bruin et al., 1999; Katul et al., 2008; Mahrt, 1991). This positive T-q correlation usually decreases with height

©2018. American Geophysical Union. All Rights Reserved.

Figure 1. A Google Earth image of the study site (32.44°N, 90.03°W) in Ross Barnett Reservoir, Ridgeland, Mississippi, United States and a picture of the eddy covariance (EC) tower looking toward the northeast.

and reverses to negative values consistent with an increase of the negative moisture skewness with height (Mahrt, 1991). The significant variability of the *T-q* correlation in the ASL and its increase with the moisture skewness indicates that entrainment of warm/dry eddies reduces the *T-q* correlation in the ASL (Mahrt, 1991). These findings suggest a link between the *T-q* correlation and boundary layer heights as the ASL turbulence is readily accessible to the entrained warm/dry eddies from the top of the boundary layer. Indeed, the temperature and humidity are less correlated in shallow marine boundary layers than in deep marine boundary layers, as indicated by Larsén et al. (2014). However, the aforementioned study attributed this feature to the stronger impact of the boundary layer-scale eddies in breaking the "same source, same sink" assumption for scalar similarity. This is consistent with a number of other studies that also suggested that the entrainment dissimilarity argument implies that the scales contributing to the weak *T-q* correlation must be commensurate with the atmospheric boundary layer height (Asanuma et al., 2007; Cava et al., 2008; Choi et al., 2004; Larsén et al., 2014).

Warm air aloft is associated with temperature inversions and stable conditions that suppress mixing; whereas cool air aloft is associated with unstable conditions that enhance mixing. While previous studies often focused on entrainment of warm/dry air parcels, how entrainment of cool/dry air parcels, instead of warm/dry air parcels, affects the ASL *T-q* dissimilarity remains a topic to be explored and frames the scope of the work here. The above overview is suggestive that when entrained cool/dry air masses characterized by a positive *T-q* correlation impinge on the ASL formed over a moist and warm water surface, *T-q* similarity in the ASL is likely to be enhanced, especially with increasing friction velocity indicating a stronger impact of large-scale eddies. This conjecture is explored using eddy covariance (EC) data collected over a large reservoir where the variability in *T-q* similarity is measured.

2. Experimental Data

2.1. Site and Instruments

The data were collected over the Ross Barnett Reservoir, Ridgeland, Mississippi, United States (Figure 1). The EC tower was positioned on a stationary wooden platform, which was located in the south center of the reservoir. The mean water depth was about 5 m, but the distance from the EC instruments to the water surface varied from 3.7 to 4.2 m with a mean value of 4 m. The distance from the tower to the shore ranged from 2 km to more than 14 km (Figure 1). The details of the reservoir, site, and instruments are documented in previous studies (Liu et al., 2009, 2012, 2016; Zhang & Liu, 2013) and are not repeated here. Briefly, the EC

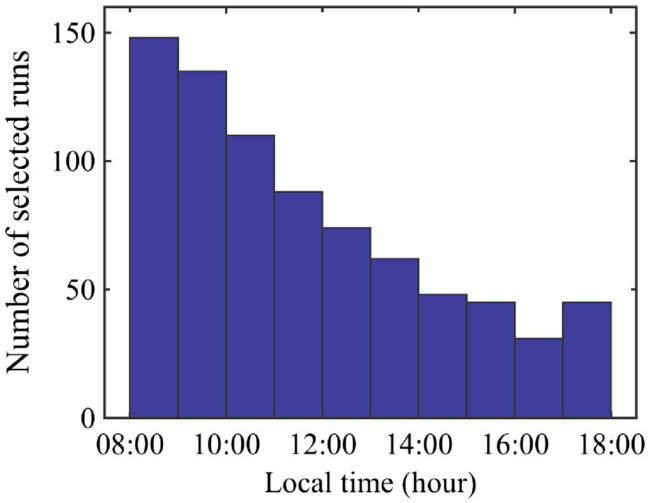

Figure 2. The number of selected runs in each hour.

system composed of a three-dimensional sonic anemometer (model CSAT3, Campbell Scientific, Inc.) and an open path gas analyzer (model LI-7500, LI-COR, Inc.) measuring longitudinal, lateral, and vertical wind velocity components (u, v, and w), T, and water vapor concentration, respectively. The time series were sampled at 10 Hz using a data logger (CR5000, Campbell Scientific, Inc.) and stored for future processing. The 10 Hz data were then processed and corrected to obtain 30-min mean turbulent fluxes following conventional postfield data processing procedures (e.g., despiking, double rotation for the sonic anemometer velocities, and corrections of sonic temperature and density applied to fluxes). After postprocessing, each 30-min averaging interval defines a run. The procedures of postprocessing are detailed elsewhere (Gao et al., 2016; Liu et al., 2009; Zhang & Liu, 2013). Other measurements include net radiation, air temperature and relative humidity, another independent mean wind speed and direction, and water temperature.

2.2. Data Selection

At night, the adjacent land surface cools more quickly than the lake water, leading to much cooler air over the land than over the water and creating an unstable ASL over the water. Shortly after sunrise, the air over the land remains cooler than the air over the water surface for several hours in the morning, despite of a faster increase in the land surface temperature when compared to the water. Thus, an unstable ASL over the water persists in the morning hours. Only in the afternoon when the land surface eventually becomes warmer than the water surface does the passage of warm air from lands over the cool water surface generate a stable ASL over water. Under the influence of large-scale cold air bursts or cold front passages under northerly winds, an unstable ASL also persists over the water and cool/dry air masses dominate (Liu et al., 2011). Thus, the data under daytime unstable conditions from the EC system over the water are used here to address the research objective. The ASL stability parameter $\zeta=z/L$ is taken to be < -0.02, where z and L are the measurement height and Obukhov length, respectively. There is a total of 4,140 thirty-minute runs for the period from August 2007 to December 2008.

In addition to the above criterion, runs were excluded when

1. Winds originated from the 80 to 280° sector because such runs were likely to be influenced by the tower and the supporting structures. Approximately 45% of the 30-min runs were excluded by this step;
2. Turbulence intensity, I_u ($I_u = \sigma_u/\overline{u}$, where $\overline{u}$ and σ_u represent the mean and standard deviation of u), was larger than 0.5 to minimize distortions arising from the usage of Taylor's frozen turbulence hypothesis. Approximately 5% of the runs left from the last step were rejected;
3. Friction velocity (u_*) and sensible and latent heat fluxes were below the following thresholds (i.e., 0.05 m s^{-1} and 5 W m^{-2}). Approximately 19% of the runs left from the last step were excluded;
4. Abnormally large spectral amplitudes of u, v, w, T, or specific humidity (q) at higher frequencies were recorded (Stull, 1988). Approximately 12% of the runs left from the last step were rejected.

Overall, 786 thirty-minute runs accounting for about 19% of the total runs were selected and analyzed. Figure 2 shows the number of selected runs in each hour. Approximately 61% of the selected runs were observed in the morning hours. Unstable conditions could persist in the afternoon under the influence of large-scale cold air bursts or cold front passages. The unstable runs in the afternoon were also included.

3. Methodology

3.1. Spectral Analysis

Using spectral analysis, previous studies suggest that the T-q similarity is highly scale dependent (Asanuma et al., 2007; Larsén et al., 2014), and the scale dependence of the T-q similarity changes largely under different stability and wind speed conditions (Larsén et al., 2014). In order to examine the scale-dependence of the T-q similarity under different wind shear conditions, we applied fast Fourier transform for each 30-min run

following Asanuma et al. (2007) and Larsén et al. (2014). The scale-dependent (spectral) correlation coefficients, $\gamma_{Tq}(n)$, between T and q are defined as

$$\gamma_{Tq}(n) = \frac{Co_{Tq}}{S_T S_q}, \tag{1}$$

where S_T and S_q are the individual power spectra of T and q, respectively, Co_{Tq} is the cospectrum between T and q, and $n = fz/U$ is the normalized frequency, with f being the frequency (in Hertz) and U the mean horizontal wind speed at z.

3.2. Hilbert Transform

To investigate the underlying cause for the T-q dissimilarity under different wind shear conditions, we calculated phase angle differences between the time series of T and q to quantify the synchronization of the two time series (Gao et al., 2017; Larsén et al., 2014; Li & Bou-Zeid, 2011). Fast Fourier transform can be used to infer the phase-angle distribution (or phase spectrum) using the Quadrature spectrum and Co_{Tq} derived from the cross spectrum of two series. However, at low frequency, the shape of the phase spectrum can be appreciably distorted by windowing and tapering prompting interest in alternative approaches. The Hilbert transform (HT) offers one such alternative and was used here to determine phase angle differences between two time series (e.g., T and q) as described elsewhere (Gao et al., 2017). Briefly, for a series $X(t)$, its HT $\widehat{X}(t)$ is given by

$$\widehat{X}(t) = \frac{1}{\pi} P \int_{-\infty}^{\infty} \frac{X(\tau)}{t-\tau} \mathrm{d}\tau, \tag{2}$$

where P is the Cauchy principle value integral. The Cauchy principle value integral is effective when a series is nonstationary and its energy content may exhibit a singularity as may be expected from a $1/f$ noise with $f \to 0$ (i.e., large scales). With the original series and its HT, an analytic signal can be constructed using

$$Z^X(t) = X(t) + i\widehat{X}(t) = A(t)e^{i\Phi(t)}, \tag{3}$$

where $i = \sqrt{-1}$, and A and Φ denote the instantaneous amplitude and phase function, respectively, given by

$$A(t) = \left(X^2 + \widehat{X}^2\right)^{\frac{1}{2}}, \tag{4}$$

$$\Phi(t) = \tan^{-1}\left(\frac{\widehat{X}}{X}\right). \tag{5}$$

The Hilbert cross spectrum of two signals $X(t)$ and $Y(t)$ is defined as

$$\mathrm{HCS}^{XY}(t) = Z^{X*}(t) \cdot Z^Y(t), \tag{6}$$

where * denotes complex conjugation. The instantaneous Hilbert phase difference between two series is determined using

$$\Phi_{\mathrm{diff}}(t) = \tan^{-1}\left(\frac{\mathrm{Im}\left[\mathrm{HCS}^{XY}(t)\right]}{\mathrm{Re}\left[\mathrm{HCS}^{XY}(t)\right]}\right), \tag{7}$$

where Im and Re are the imaginary and real parts of the Hilbert cross spectrum, respectively. Here the time-averaged absolute phase difference $|\Phi_{\mathrm{diff}}|$ is used to represent the phase difference between two series.

3.3. Quadrant Analysis

To further examine the influence of cool/dry air masses on the T-q dissimilarity under different wind shear conditions, we applied a conditional sampling method of quadrant analysis to decompose fluxes into four quadrants according to the sign of the fluctuating components (Li & Bou-Zeid, 2011; Smedman et al., 2007; Wallace, 2016). Description of quadrant events for $w'T'$, $w'q'$, and $T'q'$ are shown in Table 1. Here primed quantities denote turbulent fluctuations with respect to the time-averaged state. A hyperbolic hole (e.g., $H = 1$) is also applied to separate the relatively short-lived extreme events from the small-magnitude fluctuations (i.e., $|w'c'| > H|\overline{w'c'}|$, where $c = u$, T, or q, and overbar denotes the time average). For each quadrant k and a hole size H, the average fluxes can be calculated from

Table 1
Description of the Quadrants for $w'T'$, $w'q'$, and $T'q'$

Flux	Quadrant 1 (Q1)	Quadrant 2 (Q2)	Quadrant 3 (Q3)	Quadrant 4 (Q4)
$w'T'$	$(+w')(+T')$	$(+w')(-T')$	$(-w')(-T')$	$(-w')(+T')$
	Upward warm air	Upward cool air	Downward cool air	Downward warm air
$w'q'$	$(+w')(+q')$	$(+w')(-q')$	$(-w')(-q')$	$(-w')(+q')$
	Upward moist air	Upward dry air	Downward dry air	Downward moist air
$T'q'$	$(+T')(+q')$	$(+T')(-q')$	$(-T')(-q')$	$(-T')(+q')$
	Warm/moist air	Warm/dry air	Cool/dry air	Cool/moist air

$$\overline{w'c'}_{k|H} = \frac{1}{N}\sum_{t=1}^{N} w'c' I_{k|H}(t), \tag{8}$$

where N is the number of samples for a 30-min period, and $I_{k|H}(t) = 1$ if the tth sample falls into the quadrant k and satisfies $|w'c'| > H|\overline{w'c'}|$, otherwise $I_{k|H}(t) = 0$. The fractions of flux contribution and time occupation of each quadrant k are calculated as

$$S_{k|H} = \overline{w'c'}_{k|H}/\overline{w'c'}, \tag{9}$$

$$D_{k|H} = \frac{1}{N}\sum_{t=1}^{N} I_{k|H}(t). \tag{10}$$

Separate tests indicate that selecting different hole sizes (e.g., $H = 1$, 2, or 3) resulted in similar patterns in the distribution of $S_{k|H}$ and $D_{k|H}$ (not shown here) provided $H \geq 1$. In the following, we present the results with $H = 1$ to exclude small-magnitude fluctuations but still retain a significant number of events for statistical inferences.

4. Results and Discussion

4.1. Variability of Temperature-Humidity Similarity

The correlation coefficient between T and q, $R_{Tq} = \overline{T'q'}/(\sigma_T\sigma_q)$ where $\sigma_T = \sqrt{\overline{T'T'}}, \sigma_q = \sqrt{\overline{q'q'}}$ are the standard deviations of temperature and water vapor concentration, is often used to describe the T-q similarity. Figures 3a and 3b shows variations of R_{Tq} with $-\zeta$ and u_*, respectively, for daytime unstable conditions. Dissimilarity between T and q was evident with R_{Tq} ranging from 0.10 to 0.95 with the bin averages varying differently with $-\zeta$ and u_*. As shown in Figure 3a, R_{Tq} was relatively high for near-neutral conditions and lower and more scattered for more unstable conditions, opposite to prior results by Larsén et al. (2014) in the marine ASL under unstable conditions. Larsén et al. (2014) found that T and q were best correlated for the deepest boundary layer but poorly correlated for shallow boundary layer and attributed the variations in R_{Tq} to the combined effects of instabilities and the boundary layer depths. When R_{Tq} is plotted as a function of u_* (Figure 3b), two interesting features emerge. With the increased u_* from 0.05 m s^{-1} to about 0.4 m s^{-1}, R_{Tq} increased by about 50% on average and the scatter was reduced. These features indicate that T and q behaved similarly under higher wind shear conditions.

What were the causes leading to the improved similarity between T and q and the reduced scatter of R_{Tq} as u_* increased? Numerous studies have suggested that the reduced T-q correlations are caused by large turbulent

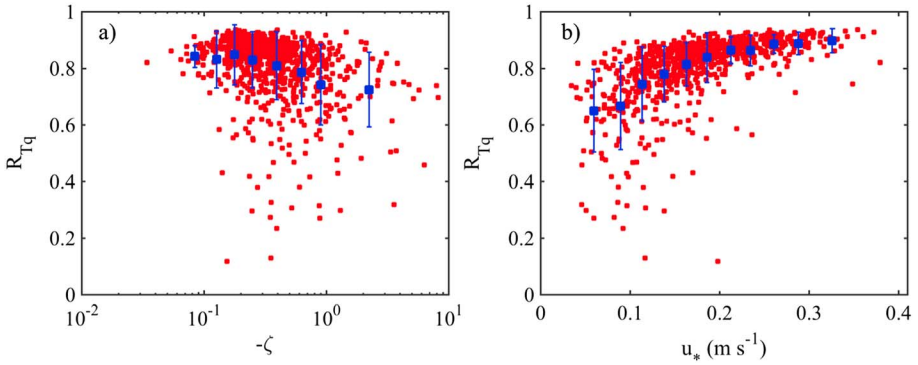

Figure 3. Variations of R_{Tq} with (a) $-\zeta$ and (b) u_*. The blue squares and bars refer to the bin averages and the corresponding standard deviations.

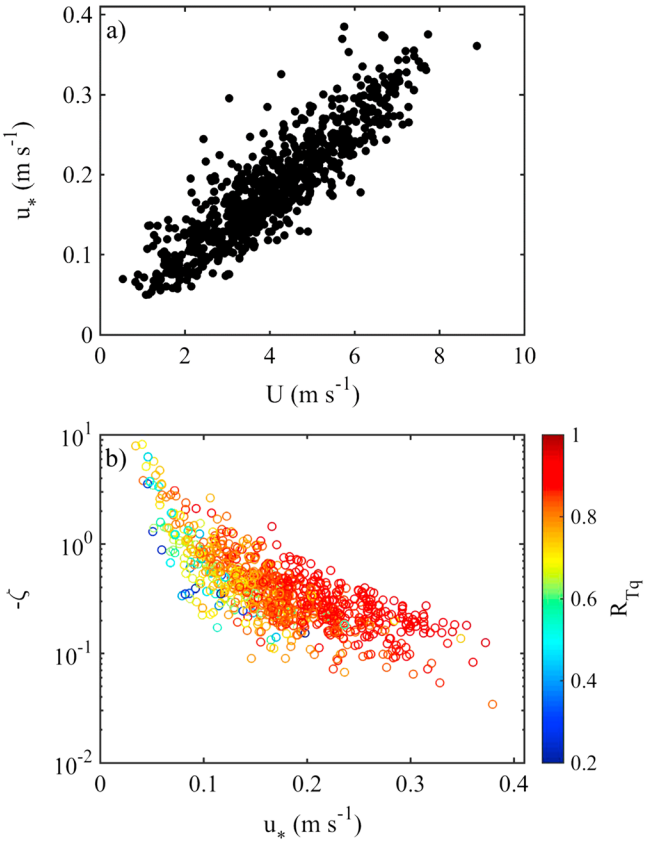

Figure 4. (a) Variations of u_* with the mean horizontal wind speed U and (b) variations of $-\zeta$ with u_* (with R_{Tq} also shown in color).

eddies and their interaction with ASL turbulence (Asanuma et al., 2007; Larsén et al., 2014; Li et al., 2012). It is hypothesized here that variability in R_{Tq} is associated with large turbulent eddies whose *T-q* correlation within those large-scale eddies increases with increasing u_*. Because increasing u_* increases the entrainment velocity of cool/dry air, a plausible explanation for the enhanced (and positive) *T-q* correlation within those large-scale eddies is the entrainment hypothesis. In other words, the increased entrainment of large-scale cool/dry eddies with a positive *T-q* correlation improves the *T-q* similarity in the ASL. The positive *T-q* correlation above the internal boundary layer formed over the water surface (where the ASL and EC measurements are embedded) is likely to be due to large-scale advection of cool/dry air mass originating from land (as described in a later section).

4.2. Influence of Wind Shear on Temperature-Humidity Similarity of Large Eddies

4.2.1. Spectral Analysis of Temperature-Humidity Similarity

As shown in Figure 4, u_* increased with the increased mean horizontal wind speed, and the instability in the ASL decreased with increased u_* as expected. Considering the two interesting features in $R_{Tq}(u_*)$, we mainly focused on the effects of wind shear on the *T-q* similarity. To make our analysis manageable and representative, the data were classified into 11 groups according to the ranges of u_* (as shown in the legend of Figure 5). The mean and standard deviation of R_{Tq} for each group are plotted in Figure 3b. Figure 5 presents the mean spectral correlation coefficients $\gamma_{Tq}(n)$ as a function of the normalized frequency $n = fz/u$ for the different ranges of u_*. These spectra can be roughly divided into two parts: (1) the middle- to low-frequency part (e.g., $n < 0.02$) where $\gamma_{Tq}(n)$ decreased as the size of turbulent eddies increased; (2) the middle- to high-frequency part (e.g., $n > 0.02$) where $\gamma_{Tq}(n)$ also leveled off as the sizes of turbulent eddies decreased. One striking feature is that in the middle- to low-frequency range, the mean $\gamma_{Tq}(n)$ spectra for the larger u_* groups had larger power magnitudes than those for the smaller u_* groups, whereas in the middle- to high-frequency range, especially in $n > 0.2$, the mean $\gamma_{Tq}(n)$ spectra for all groups had comparable magnitudes. Apparently, the enhanced $\gamma_{Tq}(n)$ spectra in the middle- to low-frequency range was the main cause leading to the observed enhancement of *T-q* similarity as u_* increased. For the smaller u_* groups, the mean $\gamma_{Tq}(n)$ spectra were also suppressed in the frequency range of $0.02 < n < 0.2$.

Improved *T-q* similarity caused by the enhanced $\gamma_{Tq}(n)$ spectrum in the middle- to low-frequency range is also consistent with prior results (Asanuma et al., 2007; Larsén et al., 2014; Li et al., 2012). By classifying their data

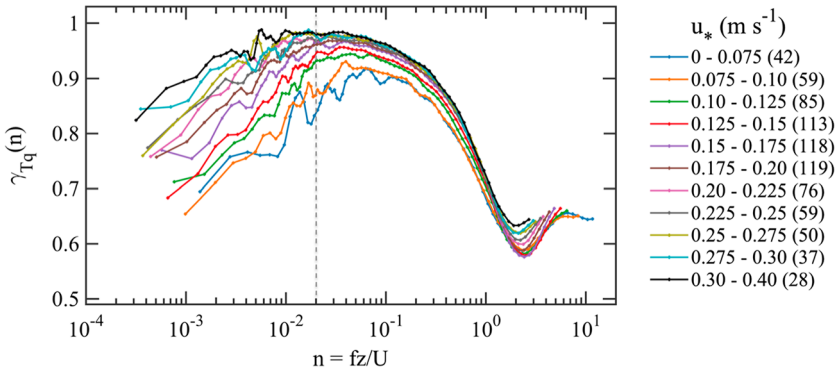

Figure 5. γ_{Tq} as a function of the normalized frequency $n = fz/U$ for different ranges of u_* as listed in the legend. The dash line refers to $n = 0.02$.

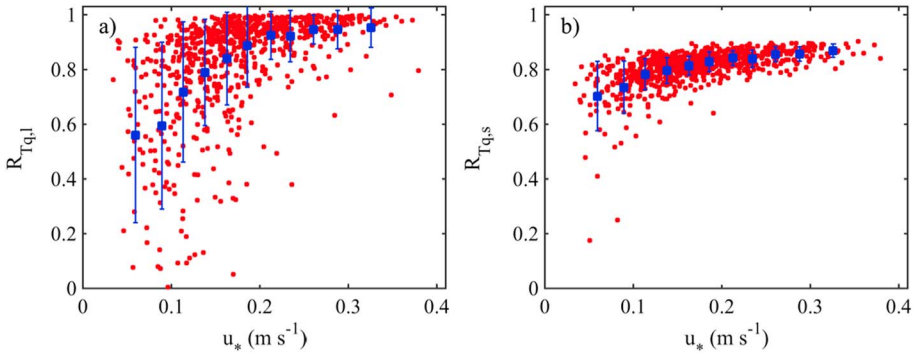

Figure 6. Variations of R_{Tq} caused by (a) large eddies and (b) small eddies with the original u_*.

into two groups with $R_{Tq} > 0.5$ and $R_{Tq} < 0.5$, respectively, Asanuma et al. (2007) illustrated that in the middle- to low-frequency range, the mean $\gamma_{Tq}(n)$ spectra for the higher-correlation group had consistently larger magnitude than those for the lower-correlation group. Li et al. (2012) also reported the reduced mean $\gamma_{Tq}(n)$ spectra in the middle-frequency range for the lower-correlation group over a lake.

4.2.2. The Temperature-Humidity Similarity of Large Eddies

To further investigate the reason for the increased *T*-*q* correlation of large eddies at higher wind shear conditions, we first extracted large eddies (i.e., low-frequency motions) of *T* and *q* from the 10 Hz time series data. While several methods have been applied to separate large eddies from small eddies (Gao et al., 2016, 2017; Katul & Vidakovic, 1998), the key question is how to identify a threshold frequency delineating large and small eddies. Over the water surface, about 2 km of fetch is guaranteed to the northwest (Figure 1). During the daytime unstable conditions, when cool/dry air flowed from the upstream land surface over the water surface, an internal boundary layer (IBL) with a depth of about one tenth the fetch (e.g., ~200 m) would develop (Bou-Zeid et al., 2004). Thus, it is reasonable to assign $n \approx 0.02$ as a threshold frequency separating large eddies from small eddies ($n \approx 0.02$ corresponds to a length scale of about 200 m). Here a Fourier-based filter is used: the scales with $n < 0.02$ in the Fourier domain were labeled as large eddies (i.e., x_l, where $x = w$, q, and T, and l refers to large eddies for x), and $n > 0.02$ as small eddies (i.e., x_s, where s refers to small eddies for x). Tests indicate that the selection of different threshold frequencies has minor effects on the results and conclusions presented here.

After separating the original time series into two subseries for large eddies and small eddies, the correlations of $R_{Tq,l}$ and $R_{Tq,s}$ associated with large eddies and small eddies, respectively, can be calculated. Their variations with u_* are presented in Figure 6. $R_{Tq,l}$ exhibited a larger variability than $R_{Tq,s}$ and even greater than R_{Tq} itself as u_* increased. On average, $R_{Tq,l}$ increased by about 70% and had large scatter, whereas $R_{Tq,s}$ increased by only about 24% and had small scatter. For large eddies, temperature and humidity fluctuations became more similar to each other (i.e., $R_{Tq,l}$ close to unity) under higher wind shear conditions. For small eddies, the averaged $R_{Tq,s} = 0.81$. Naturally, smaller eddies are more impacted by sensor separation distances and we cannot confirm whether $R_{Tq,s} = 0.81$ was a significant deviation from unity at fine scales or simply an artifact of sensor separation. However, what is not in dispute is that the enhancement rate of $R_{Tq,l}$ with increased u_* was primarily associated with large eddies.

It is apparent that large eddies played a central role in the temperature and humidity similarity. Why large eddies of *T* and *q* became more correlated with the increased wind shear motivated further exploration. Larsén et al. (2014) studied the Fourier phase spectra between *T* and *q* and found that in the middle- to low-frequency range, the phase difference between *T* and *q* exhibited a larger scatter when *T* and *q* become less correlated. In the next section, we examined how an increase in wind shear affected the phase angle difference between large eddies of *T* and those of *q*.

4.2.3. The Phase Difference Between Temperature and Humidity of Large Eddies

As described in section 3.3, the HT was applied to calculate the phase differences between large eddies of *T* and those of *q* as well as between small eddies of *T* and those of *q*. When warm/moist air parcels (cool/dry air parcels) move upward (downward), for example, *T* and *q* are considered to be perfectly in phase (i.e., phase difference $|\Phi_{diff}| = 0°$). When warm/dry air parcels (cool/moist air parcels) move upward (downward), *T* and *q*

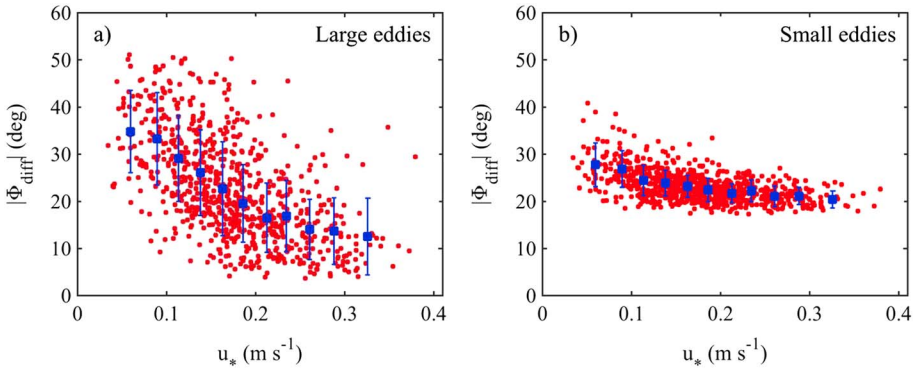

Figure 7. Variations of mean absolute phase difference ($|\Phi_{diff}|$) between T and q with u_* for (a) large eddies and (b) small eddies.

are considered to be perfectly out-of-phase (i.e., $|\Phi_{diff}|$= 180°). As shown in Figure 7, the phase differences between large eddies of T and those of q had a larger scatter with $|\Phi_{diff}|$ varying from 0 to 50°, as compared to $|\Phi_{diff}|$ for small eddies (i.e., 18~40°). For large eddies of T and q, their phase differences decreased appreciably with the increased wind shear (Figure 7a), suggesting an improved "synchronization" between T and q of large eddies as u_* increased (i.e., not time lags). For small eddies (Figure 7b), however, $|\Phi_{diff}|$ decreased within a narrow range (Gao et al., 2017; Larsén et al., 2014; Li & Bou-Zeid, 2011). These results further confirm the patterns and trends in Figures 5 and 6, although there was an obvious link between correlation coefficient and phase difference between two variables. However, why would large eddies of T and q become more synchronized as wind shear increased? As shown next, the answer lies in the already established positive correlation for cool/dry air parcels existing above the IBL and the enhanced sweeping component with the increasing u_*.

4.3. Linking Temperature-Humidity Similarity to Entrainment Processes

Figure 8 shows the quadrant analysis of $w'T'$, $w'q'$, and $T'q'$ with respect to u_*. In general, the behavior of each quadrant was almost the same for $w'T'$ and $w'q'$ (i.e., Figure 8a versus Figure 8c, and Figure 8b versus Figure 8d). At lower wind shear conditions, each quadrant of $T'q'$ exhibited a relatively larger scatter, and warm/dry (Q2) and cool/moist (Q4) air also accounted for very small fractions of covariances and time durations (Figures 8e and 8f), corresponding to the observed larger scatter and lower correlations between T and q in Figures 3b and 6a. At higher wind shear conditions, Q2 and Q4 of $T'q'$ only contributed very limited fractions of covariances and time durations with less scatter, suggesting that large-scale temperature and humidity fluctuations were more synchronized, consistent with the results in the previous sections.

As shown in Figures 8a and 8c, Q1 and Q3 contributed the first (about 70%) and second (about 30%) largest part of the heat and water vapor fluxes (with small negative contributions from Q2 and Q4), accounting for more than 15% of the total time durations, respectively. Therefore, over the water surface, the daytime unstable ASL was statistically predominated by large upward warm/moist (Q1) and downward cool/dry (Q3) large eddies. It is interesting to note that for Q1 of $w'T'$ and $w'q'$, their fluxes and time fractions remained almost constant as u_* increased; whereas for Q3, their fluxes and time fractions increased by 10% ($P < 0.0001$) and 2% ($P < 0.0001$), respectively, with the increased wind shear. The linear regression coefficients for each quadrant are presented in Table 2. Prior studies have shown that these downward cool/dry large eddies are linked to entrainment processes over water surfaces, leading to largely enhanced latent heat fluxes (Blanken et al., 2003). These features suggest that entrainment of cool/dry large eddies was enhanced with the increased wind shear during the daytime unstable conditions. The variations of quadrant analysis for $T'q'$ with u_* (Figures 8e and 8f) further confirm these results. Both fluxes and time fractions of $T'q'$ caused by downward cool/dry eddies (Q3) were increased significantly ($P < 0.0001$) with the increased wind shear; whereas the flux fractions of $T'q'$ caused by upward warm/moist eddies (Q1) decreased. In addition, as u_* increased, the negative flux contributions from upward cool/dry (Q2) and downward warm/moist (Q4) eddies increased slightly, which were accompanied by an increase in their time fractions, leading to a decrease in the correlations of R_{wT} and R_{wq} (not shown here).

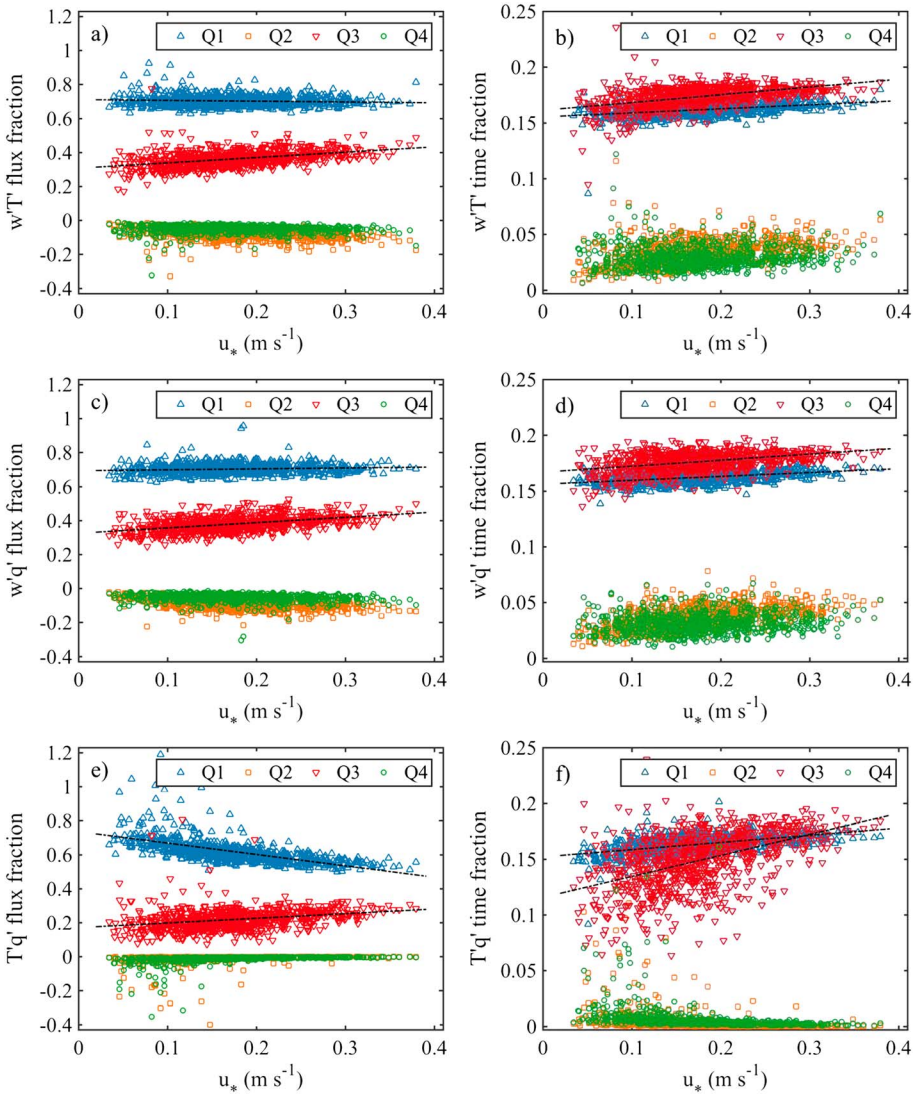

Figure 8. Variations of flux and time fractions of four quadrant events with u_* for (a and b) w'-T', (c and d) w'-q', and (e and f) T'-q'.

4.4. A Schematic Overview

For daytime unstable conditions, it is expected that upward warm/moist air masses were the dominant transporting structures (Figure 9), with nearly constant flux contribution and time fractions as u_* increased (Figure 8). For low u_* (Figure 9a), the coherence of the advected cool/dry eddies from land was uneven or

Table 2
Linear Regression Coefficients for the Flux Contribution (S_i, Where i=1, 2, 3, and 4 Refer to Four Different Quadrants) and Time Fraction (D_i) for Each Quadrant of $w'T'$, $w'q'$, and $T'q'$ With Friction Velocity

		Q1		Q2		Q3		Q4	
		Intercept	Slope	Intercept	Slope	Intercept	Slope	Intercept	Slope
$w'T'$	S_i	**0.712**	−0.046	**−0.052**	**0.159**	**0.308**	**0.314**	**0.048**	−0.014
	D_i	**0.156**	**0.036**	**0.021**	**0.070**	**0.162**	**0.068**	**0.027**	0.013
$w'q'$	S_i	**0.695**	0.054	**−0.049**	**−0.222**	**0.326**	**0.312**	**−0.045**	**−0.057**
	D_i	**0.156**	**0.035**	**0.022**	**0.080**	**0.167**	**0.053**	**0.027**	**0.025**
$T'q'$	S_i	**0.737**	**−0.671**	**−0.033**	**0.123**	**0.172**	**0.274**	**−0.041**	**0.149**
	D_i	**0.152**	**0.064**	**0.014**	**−0.051**	**0.116**	**0.189**	**0.017**	**−0.058**

Note. Numbers in bold font indicate statistically significant with $P < 0.0001$.

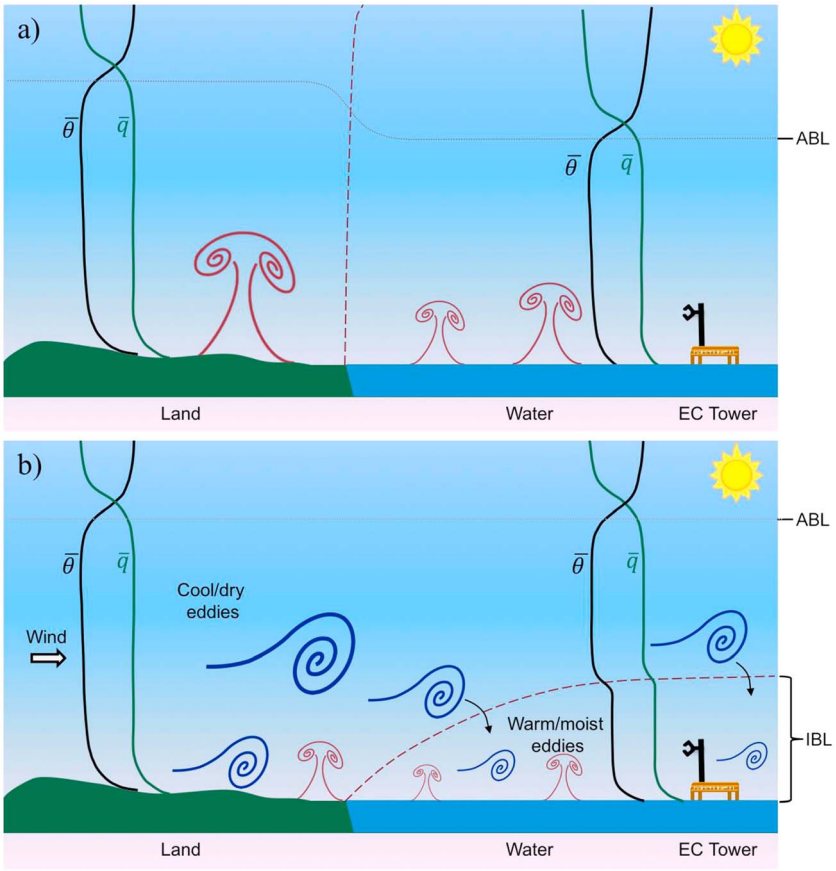

Figure 9. Schematic diagrams of entrainment processes over a water surface for (a) low u_* and (b) high u_* conditions. Turbulent eddies in red and blue represent upward warm/moist air masses and shear-generated large eddies, respectively. Idealized virtual potential temperature ($\overline{\theta}$) and water vapor mixing ratio ($\overline{q}$) profiles over land and water are also shown. Note that the dimensions in the two panels are not proportionally scaled. EC = eddy covariance; IBL = internal boundary layer; ABL = atmospheric boundary layer.

nonexistent altogether, leading to increased phase differences and thus degraded similarity between large eddies of T and q. Indirect evidence for this postulate was that entrained cool/dry eddies would be limited, as reflected by the small time fractions of Q3 (Figure 8). Such uneven variations in heat and water vapor similarity in the large eddies impinging on the ASL resulted in large scatter in R_{Tq} and a degraded T-q correlations (Figure 3b).

Large winds may have advected from land well-correlated T and q eddies above the IBL (Figure 9b) and strong entrainment fluxes into the IBL. Along with the energetic nature of large eddies, these entrained, already well-correlated large eddies experienced less distortions in their T and q similarity before they impinged the ASL. Thus, both flux and time fractions of downward cool/dry eddies (Q3) were enlarged (Figure 8), and T and q were more correlated under higher wind shear conditions (Figure 3b). Note that the effects of horizontal advection are also likely enhanced with increases in wind speeds (or u_*), enhancing sensible and latent heat exchange, and thus strengthening T-q correlations.

5. Conclusions

Using data measured over an inland water surface, the impacts of large eddies on the temperature-humidity similarity were analyzed. With the increase in wind shear, R_{Tq} increased and its degree of scatter decreased remarkably. Both spectral and statistical analysis proved that large eddies were largely responsible for the enhanced T-q correlations under high wind conditions. Large eddies of T and q became more correlated and synchronized with the increased winds. As u_* increased, the phase difference between large eddies of T and q exhibited a noticeable decreasing trend. The quadrant analysis suggests that the enhanced R_{Tq} with the increased u_* was likely to be caused by the enhanced entrainment of large cool/dry eddies with more

synchronized attributes of T and q under high winds. The analysis also suggests that the well-corrected, energetic large eddies transporting T and q under high wind conditions penetrated the IBL and contributed to the observed high T-q similarity in the ASL, as compared with low wind conditions. While entrainment velocity is expected to scale with u_* for near-neutral conditions, it is unclear whether such enhanced scalar entrainment was associated with a shallow or deep IBL, a topic to be explored in the future. It should be stressed that though this study was conducted over a water surface, the major conclusions should hold over vegetated surfaces with the influence of cool/dry air advection and entrainment when the sensible and latent heat fluxes remain both positive.

Acknowledgments
Liu and Katul acknowledge support from the National Science Foundation (NSF-AGS-1419614, NSF-AGS-1112938, NSF-EAR-1344703, NSF-AGS-1644382, NSF-IOS-1754893, and NSF-DGE-1068871) and from the Department of Energy (DE-SC0011461). We thank Dan Gaillet, Billy Lester, Jason Temple, and staff in Pearl River Valley Water Supply District in Ridgeland, Mississippi, as well as Yu Zhang, Haimei Jiang, Li Sheng, Rongping Li, Yu Wang, and Guo Zhang who contributed to field work. We thank two anonymous reviewers for their constructive comments. The data set used in this study are deposited in a public domain repository (https://doi.org/10.6084/m9.figshare.5686675).

References

Andreas, E. L., Hill, R. J., Gosz, J. R., Moore, D. I., Otto, W. D., & Sarma, A. D. (1998). Statistics of surface-layer turbulence over terrain with metre-scale heterogeneity. *Boundary-Layer Meteorology*, *86*(3), 379–408. https://doi.org/10.1023/A:1000609131683

Asanuma, J., Tamagawa, I., Ishikawa, H., Ma, Y., Hayashi, T., Qi, Y., & Wang, J. (2007). Spectral similarity between scalars at very low frequencies in the unstable atmospheric surface layer over the Tibetan plateau. *Boundary-Layer Meteorology*, *122*(1), 85–103. https://doi.org/10.1007/s10546-006-9096-y

Assouline, S., Tyler, S. W., Tanny, J., Cohen, S., Bou-Zeid, E., Parlange, M. B., & Katul, G. G. (2008). Evaporation from three water bodies of different sizes and climates: Measurements and scaling analysis. *Advances in Water Resources*, *31*(1), 160–172. https://doi.org/10.1016/j.advwatres.2007.07.003

Blanken, P. D., Rouse, W. R., & Schertzer, W. M. (2003). Enhancement of evaporation from a large northern lake by the entrainment of warm, dry air. *Journal of Hydrometeorology*, *4*(4), 680–693. https://doi.org/10.1175/1525-7541(2003)004%3C0680:EOEFAL%3E2.0.CO;2

Bou-Zeid, E., Meneveau, C., & Parlange, M. B. (2004). Large-eddy simulation of neutral atmospheric boundary layer flow over heterogeneous surfaces: Blending height and effective surface roughness. *Water Resources Research*, *40*, W02505. https://doi.org/10.1029/2003WR002475

Cava, D., Katul, G. G., Sempreviva, A. M., Giostra, U., & Scrimieri, A. (2008). On the anomalous behaviour of scalar flux–variance similarity functions within the canopy sub-layer of a dense alpine forest. *Boundary-Layer Meteorology*, *128*(1), 33–57. https://doi.org/10.1007/s10546-008-9276-z

Choi, T., Hong, J., Kim, J., Lee, H., Asanuma, J., Ishikawa, H., et al. (2004). Turbulent exchange of heat, water vapor, and momentum over a Tibetan prairie by eddy covariance and flux variance measurements. *Journal of Geophysical Research*, *109*, D21106. https://doi.org/10.1029/2004JD004767

de Bruin, H. A. R., Van Den Hurk, B. J. J. M., & Kroon, L. J. M. (1999). On the temperature-humidity correlation and similarity. *Boundary-Layer Meteorology*, *93*(3), 453–468. https://doi.org/10.1023/A:1002071607796

Detto, M., Katul, G., Mancini, M., Montaldo, N., & Albertson, J. D. (2008). Surface heterogeneity and its signature in higher-order scalar similarity relationships. *Agricultural and Forest Meteorology*, *148*(6-7), 902–916. https://doi.org/10.1016/j.agrformet.2007.12.008

Gao, Z., Liu, H., Katul, G. G., & Foken, T. (2017). Non-closure of the surface energy balance explained by phase difference between vertical velocity and scalars of large atmospheric eddies. *Environmental Research Letters*, *12*(3), 034025. https://doi.org/10.1088/1748-9326/aa625b

Gao, Z., Liu, H., Russell, E. S., Huang, J., Foken, T., & Oncley, S. P. (2016). Large eddies modulating flux convergence and divergence in a disturbed unstable atmospheric surface layer. *Journal of Geophysical Research: Atmospheres*, *121*, 1475–1492. https://doi.org/10.1002/2015JD024529

Guo, X., Zhang, H., Cai, X., Kang, L., Zhu, T., & Leclerc, M. (2009). Flux-variance method for latent heat and carbon dioxide fluxes in unstable conditions. *Boundary-Layer Meteorology*, *131*(3), 363–384. https://doi.org/10.1007/s10546-009-9377-3

Högström, U. (1990). Analysis of turbulence structure in the surface layer with a modified similarity formulation for near neutral conditions. *Journal of the Atmospheric Sciences*, *47*(16), 1949–1972. https://doi.org/10.1175/1520-0469(1990)047%3C1949:AOTSIT%3E2.0.CO;2

Huang, J., Katul, G. G., & Albertson, J. (2013). The role of coherent turbulent structures in explaining scalar dissimilarity within the canopy sublayer. *Environmental Fluid Mechanics*, *13*(6), 571–599. https://doi.org/10.1007/s10652-013-9280-9

Katul, G. G., & Parlange, M. B. (1994). On the active-role of temperature in surface-layer turbulence. *Journal of the Atmospheric Sciences*, *51*(15), 2181–2195. https://doi.org/10.1175/1520-0469(1994)051<2181:OTAROT>2.0.CO;2

Katul, G. G., Goltz, S. M., Hsieh, C.-I., Cheng, Y., Mowry, F., & Sigmon, J. (1995). Estimation of surface heat and momentum fluxes using the flux-variance method above uniform and non-uniform terrain. *Boundary-Layer Meteorology*, *74*(3), 237–260. https://doi.org/10.1007/BF00712120

Katul, G. G., Li, D., Liu, H., & Assouline, S. (2016). Deviations from unity of the ratio of the turbulent Schmidt to Prandtl numbers in stratified atmospheric flows over water surfaces. *Physical Review Fluids*, *1*(3), 034401. https://doi.org/10.1103/PhysRevFluids.1.034401

Katul, G. G., Sempreviva, A., & Cava, D. (2008). The temperature–humidity covariance in the marine surface layer: A one-dimensional analytical model. *Boundary-Layer Meteorology*, *126*(2), 263–278. https://doi.org/10.1007/s10546-007-9236-z

Katul, G. G., & Vidakovic, B. (1998). Identification of low-dimensional energy containing/flux transporting eddy motion in the atmospheric surface layer using wavelet thresholding methods. *Journal of the Atmospheric Sciences*, *55*(3), 377–389. https://doi.org/10.1175/1520-0469(1998)055%3C0377:IOLDEC%3E2.0.CO;2

Larsén, X., Kelly, M., & Sempreviva, A. (2014). On the temperature and humidity dissimilarity in the marine surface layer. *Boundary-Layer Meteorology*, *151*(2), 273–291. https://doi.org/10.1007/s10546-013-9896-9

Lee, X., Yu, Q., Sun, X., Liu, J., Min, Q., Liu, Y., & Zhang, X. (2004). Micrometeorological fluxes under the influence of regional and local advection: A revisit. *Agricultural and Forest Meteorology*, *122*(1–2), 111–124. https://doi.org/10.1016/j.agrformet.2003.02.001

Li, D., & Bou-Zeid, E. (2011). Coherent structures and the dissimilarity of turbulent transport of momentum and scalars in the unstable atmospheric surface layer. *Boundary-Layer Meteorology*, *140*(2), 243–262. https://doi.org/10.1007/s10546-011-9613-5

Li, D., Bou-Zeid, E., & De Bruin, H. R. (2012). Monin–Obukhov similarity functions for the structure parameters of temperature and humidity. *Boundary-Layer Meteorology*, *145*(1), 45–67. https://doi.org/10.1007/s10546-011-9660-y

Liu, H., Blanken, P. D., Weidinger, T., Nordbo, A., & Vesala, T. (2011). Variability in cold front activities modulating cool-season evaporation from a southern inland water in the USA. *Environmental Research Letters*, *6*(2), 024022. https://doi.org/10.1088/1748-9326/6/2/024022

Liu, H., Zhang, Q., & Dowler, G. (2012). Environmental controls on the surface energy budget over a large southern inland water in the United States: An analysis of one-year eddy covariance flux data. *Journal of Hydrometeorology*, *13*(6), 1893–1910. https://doi.org/10.1175/JHM-D-12-020.1

Liu, H., Zhang, Q., Katul, G. G., Cole, J. J., Chapin, F. S. III, & MacIntyre, S. (2016). Large CO_2 effluxes at night and during synoptic weather events significantly contribute to CO_2 emissions from a reservoir. *Environmental Research Letters*, *11*(6), 064001. https://doi.org/10.1088/1748-9326/11/6/064001

Liu, H., Zhang, Y., Liu, S., Jiang, H., Sheng, L., & Williams, Q. L. (2009). Eddy covariance measurements of surface energy budget and evaporation in a cool season over southern open water in Mississippi. *Journal of Geophysical Research*, *114*, D04110. https://doi.org/10.1029/2008JD010891

Mahrt, L. (1991). Boundary-layer moisture regimes. *Quarterly Journal of the Royal Meteorological Society*, *117*(497), 151–176. https://doi.org/10.1002/qj.49711749708

McNaughton, K. G., & Laubach, J. (1998). Unsteadiness as a cause of non-equality of eddy diffusivities for heat and vapour at the base of an advective inversion. *Boundary-Layer Meteorology*, *88*(3), 479–504. https://doi.org/10.1023/A:1001573521304

Moene, A., & Schüttemeyer, D. (2008). The effect of surface heterogeneity on the temperature–humidity correlation and the relative transport efficiency. *Boundary-Layer Meteorology*, *129*(1), 99–113. https://doi.org/10.1007/s10546-008-9312-z

Smedman, A.-S., Högström, U., Hunt, J. C. R., & Sahlée, E. (2007). Heat/mass transfer in the slightly unstable atmospheric surface layer. *Quarterly Journal of the Royal Meteorological Society*, *133*(622), 37–51. https://doi.org/10.1002/qj.7

Stull, R. B. (1988). *An introduction to boundary layer meteorology*. Dordrecht, Netherlands: Kluwer Academic Publishers. https://doi.org/10.1007/978-94-009-3027-8

van de Boer, A., Moene, A. F., Graf, A., Schüttemeyer, D., & Simmer, C. (2014). Detection of entrainment influences on surface-layer measurements and extension of Monin–Obukhov similarity theory. *Boundary-Layer Meteorology*, *152*(1), 19–44. https://doi.org/10.1007/s10546-014-9920-8

Wallace, J. M. (2016). Quadrant analysis in turbulence research: History and evolution. *Annual Review of Fluid Mechanics*, *48*(1), 131–158. https://doi.org/10.1146/annurev-fluid-122414-034550

Williams, C. A., Scanlon, T. M., & Albertson, J. D. (2007). Influence of surface heterogeneity on scalar dissimilarity in the roughness sublayer. *Boundary-Layer Meteorology*, *122*(1), 149–165. https://doi.org/10.1007/s10546-006-9097-x

Zhang, Q., & Liu, H. (2013). Interannual variability in the surface energy budget and evaporation over a large southern inland water in the United States. *Journal of Geophysical Research: Atmospheres*, *118*, 4290–4302. https://doi.org/10.1002/jgrd.50435